

Miniaturized Spectrometers with a Tunable van der Waals Junction

Hoon Hahn Yoon,^{1,2,*} Henry A. Fernandez,^{1,2} Fedor Nigmatulin,^{1,2}
Weiwei Cai,³ Zongyin Yang,⁴ Hanxiao Cui,⁵ Faisal Ahmed,¹ Xiaoqi Cui,^{1,2}
Md Gius Uddin,^{1,2} Ethan D. Minot,⁶ Harri Lipsanen,¹ Kwanpyo Kim,⁷
Pertti Hakonen,² Tawfique Hasan,⁸ Zhipei Sun^{1,2,*}

¹Department of Electronics and Nanoengineering, Aalto University, Espoo 02150, Finland

²QTF Centre of Excellence, Department of Applied Physics, Aalto University,
Aalto 00076, Finland

³Key Lab of Education Ministry for Power Machinery and Engineering,
School of Mechanical Engineering, Shanghai Jiao Tong University, Shanghai 200240, China

⁴College of Information Science and Electronic Engineering,
State Key Laboratory of Modern Optical Instrumentation,
Zhejiang University, Hangzhou 310027, China

⁵School of Aeronautics and Astronautics, Sichuan University, Chengdu 610065, China

⁶Department of Physics, Oregon State University, Corvallis, Oregon 97331, United States

⁷Department of Physics, Yonsei University, Seoul 03722, Republic of Korea

⁸Cambridge Graphene Centre, University of Cambridge, Cambridge CB3 0FA, UK

*To whom correspondence should be addressed;

E-mail: `hoonhahn.yoon@aalto.fi` and `zhipei.sun@aalto.fi`

Miniaturized computational spectrometers, which can obtain incident spectra using a combination of device spectral response and reconstruction algorithm, are essential for on-chip and implantable applications. Highly-sensitive spectral measurement using a single detector allows the footprints of such spectrometers to be scaled down while achieving spectral resolution approach-

ing that of benchtop systems. We report a high-performance computational spectrometer based on a single van der Waals junction with an electrically-tunable transport-mediated spectral response. We achieve high peak wavelength accuracy (~ 0.36 nm), high spectral resolution (~ 3 nm), broad operation bandwidth (from ~ 405 to 845 nm), and proof-of-concept spectral imaging. Our approach provides a route towards ultra-miniaturization and offers unprecedented performance in accuracy, resolution, and operation bandwidth for single-detector computational spectrometers.

Spectrometers are indispensable for various applications, including industrial inspection, chemical/biological characterization, and image sensing/analysis (1, 2). Their miniaturization with high spectral resolution and wide operation bandwidth is highly desirable to meet the emerging and future demands in portable and on-chip applications (1). However, conventional spectroscopy systems typically rely on bulky dispersive optical components (e.g., gratings) and detector or filter arrays, which impose strict restrictions on ultra-miniaturization (2).

Common spectrometer miniaturization approaches therefore replace the functions of these dispersive optical elements through various schemes (Fig. S1), including photonic crystals (3), metasurfaces (4), and compact interferometers (5). Recently, a profound technological leap has seen the emergence of miniaturized computational spectrometers, which leverage the power of mathematical algorithms for spectrum reconstruction (1). Examples of such approaches have used quantum dot filter arrays on top of the charged-coupled device sensor (6), bandgap engineered multiple nanowires (7), a single nanowire with bandgap gradation (8), Stark effect in black phosphorus (9), in situ perovskite modulation (10), and a single superconducting nanowire with tunable quantum efficiency (11). However, the performance and usability of these computational spectrometers remain limited: spectral resolution and operation bandwidth are typically restricted by the number of integrated detectors (6–8), bandgap modulation limits (9, 10), and

cryogenic operational requirements (11).

Photodetection with two-dimensional (2D) layered materials is advantageous due to their strong light-matter interaction, atomically-sharp interface, and electrically-tunable photoresponse (12–14). However, insufficient band structure modulation makes it challenging to achieve high-resolution, broadband spectral sensing using a single 2D material. On the other hand, 2D materials-based van der Waals (vdW) junctions offer highly tunable functionalities beyond the constituent materials (15–17) and could overcome these limitations. In particular, we suggest that wavelength-dependent photodetection with vdW junctions recently exploited for optoelectronic logic computing (18, 19) and color sensing (20, 21) could also be key to high-resolution computational spectral sensing.

Here, we demonstrate a high-performance ultra-miniaturized computational spectrometer utilizing a single vdW junction with an electrically-tunable transport-mediated spectral response. Our device, with its footprint defined by the junction size ($\sim 22 \times 8 \mu\text{m}^2$) shows unprecedented performance for a single detector computational spectrometer, with the ability to resolve peak monochromatic wavelengths with ~ 0.36 nm accuracy, reconstruct broadband spectra with ~ 3 nm resolution, and acquire spectral images by scanning. Our single-junction spectrometer concept can be extended to other tunable junctions for achieving high spectral resolution and broad operation bandwidth with its ultra-compact size, representing the ultimate miniaturization strategy without sacrificing spectrometer performance.

The performance of computational spectrometers relies on the variability of their wavelength-dependent photoresponsivity (1, 6–11). The single-detector miniaturized spectrometers reported thus far are limited by their performance (9, 10) and usability (9, 11) due to the limited band structure modulation and consequently, the spectral response. In contrast, electrical tuning of the interfacial band alignment of a vdW junction (Fig. 1A, upper panel) enables controllable and unique interlayer transport (15–17). This allows a tunable spectral response (Fig. 1A, lower

panel) with high sensitivity and variability over a wide spectral range (12–14). This suggests that a single-vdW-junction spectrometer could achieve significantly higher performance than previously reported spectrometers (section ST1 and table S1). We combine an electrically-tunable single-vdW-junction with computational reconstruction algorithms for various applications (Fig. 1B). To experimentally realize our spectrometer concept, the following three steps are required (Fig. S2): measuring the gate-tunable spectral responses with multiple known incident spectra (learning process); measuring the gate-tunable photocurrent of the unknown incident light to be analyzed (testing process); and computing the spectral information of the

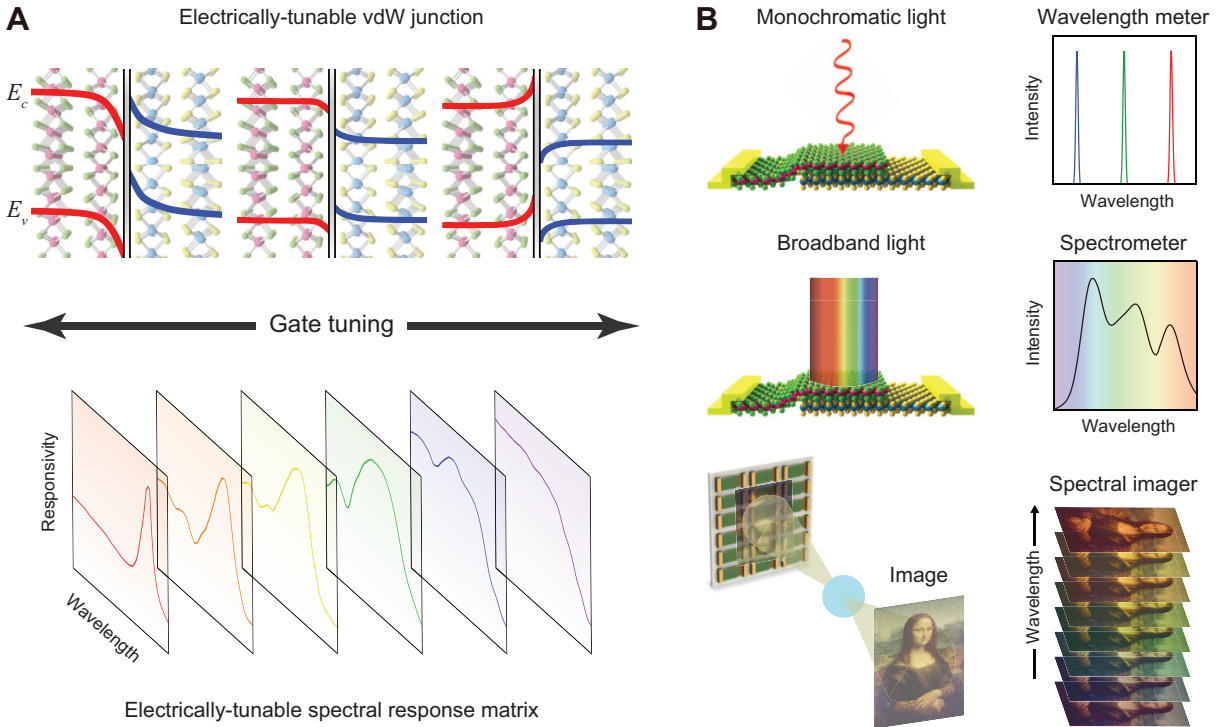


Figure 1: **Ultra-miniaturized spectrometer concept with a single-vdW-junction.** **A**, A typical gate-tunable band alignment at the vdW junction interface (upper) with its distinct gate-tunable spectral response matrix (lower). E_C (E_V) represents the conduction (valence) band edge. **B**, Schematic of various application examples using single-junction spectrometer: wavelength meter to distinguish peak wavelengths of monochromatic light (upper), spectrometer to resolve broadband spectra (middle), and spectral imager to analyze spectral information of images (lower).

unknown incident light based on the results obtained in learning and testing processes with the reconstruction algorithm (reconstructing process).

The distinct and varied photoresponse of a vdW junction, tuned at different gate voltages and incident light wavelengths, is critical to our spectrometer (*I*). We choose a MoS₂/WSe₂ heterojunction (Fig. 2A) as an example for its distinct spectral response due to the gate-tunable photovoltaic effect from the visible to the near-infrared. (22–28) The MoS₂/WSe₂ heterojunction is encapsulated by top and bottom h-BN layers for insulation and passivation, respectively (section MM1). A monolayer graphene film below the stack is used as a local gate electrode for effective gate tuning. Each stacking layer was characterized by Raman spectroscopy and atomic force microscopy (Fig. S3) to confirm the quality of the vdW heterostructure.

The transfer curves (drain-source current I_{DS} as a function of the gate-source voltage V_{GS}) of the MoS₂ or WSe₂ channels and their heterojunction are measured at drain-source voltage $V_{DS} = 3$ V in dark condition (Fig. 2B). The individual MoS₂ and WSe₂ channels exhibit n(p)-type characteristics due to the donor (acceptor) impurities in MoS₂ (WSe₂). Thus, a depletion region and built-in electric field are expected at their vdW interface (22–28). The MoS₂/WSe₂ heterojunction is characterized by positive V_{DS} applied to the WSe₂ side, corresponding to the forward biasing of the diode. The sign change of transconductance, $\frac{dI_{DS}}{dV_{GS}}$, occurs at $V_{GS} = \sim -5$ V, matching the hole current from WSe₂ with the electron current from MoS₂. This “anti-ambipolar” behavior and other transport properties (Figs. S4 to S7) are typical of the MoS₂/WSe₂ heterojunctions (22–28), providing clearly distinguishable V_{GS} -dependence.

The transfer curves of the MoS₂/WSe₂ heterojunction measured under multiple known incident lights with a bandwidth of ~ 10 nm indicate a strong wavelength dependence (Fig. 2C). The photoresponsivity, $R = \frac{I_{ph}}{P}$, measured at different V_{GS} and incident light wavelengths is used to encode the spectral response matrix, where the photocurrent is defined as $I_{ph} = I_{light} - I_{dark}$, with I_{light} and I_{dark} representing I_{DS} with and without light illumination at $V_{DS} = 3$ V, respec-

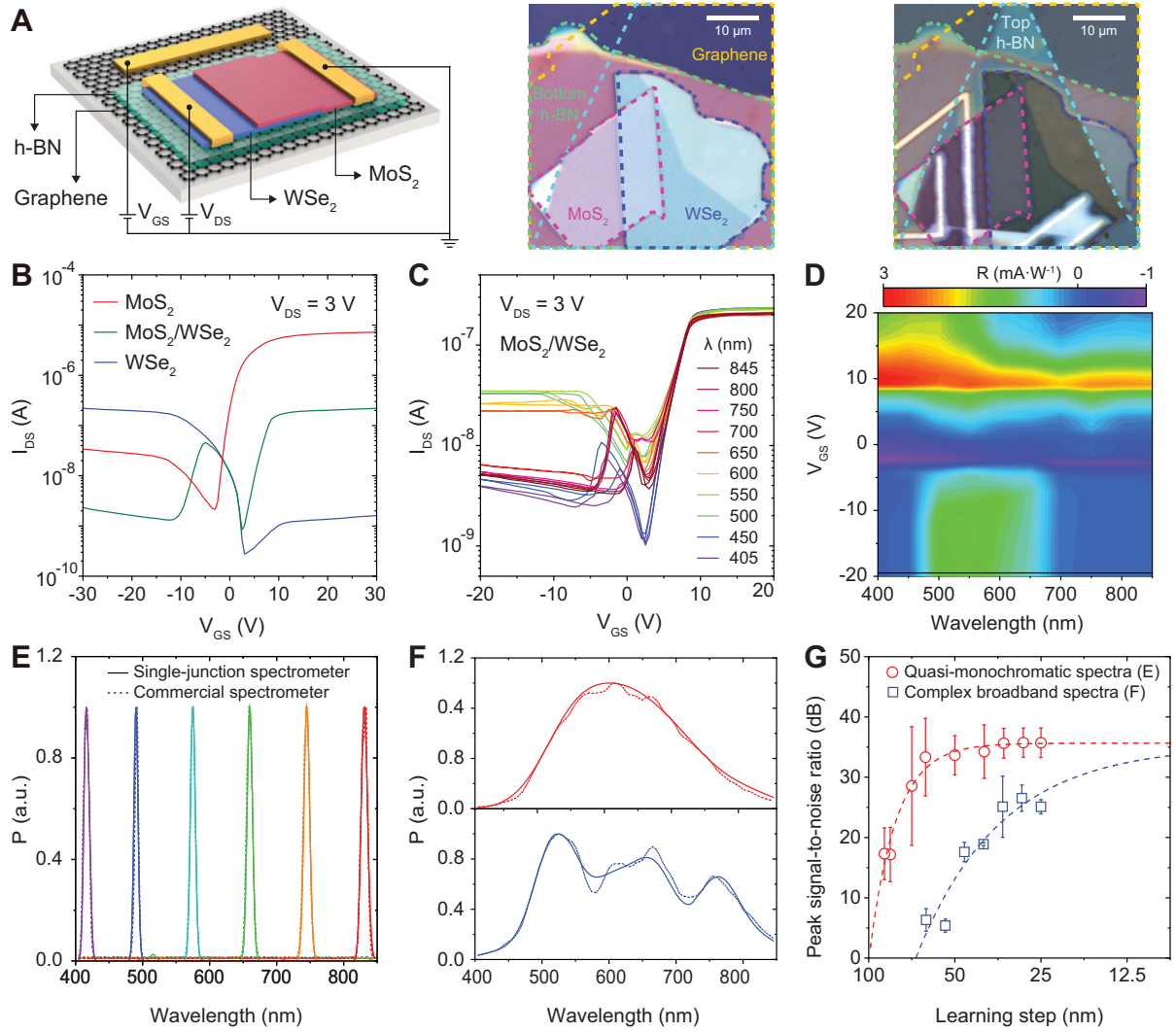


Figure 2: Single-junction spectrometer demonstration. **A**, Schematic of our MoS₂/WSe₂ heterojunction spectrometer (left) and its optical images on the h-BN and graphene layers before (middle) and after (right) depositing electrodes and stacking the top h-BN passivation layer. The top h-BN layer is not present in the upper panel for better visibility. **B** and **C**, Transfer curves of the MoS₂ and WSe₂ channels and their heterojunction with the graphene gate without (**B**) and with (**C**) light illumination at different wavelengths with a fixed power of $\sim 20 \mu\text{W}$. **D**, Color contour plot of the spectral response matrix. **E** and **F**, Quasi-monochromatic (**E**, bandwidth: $\sim 10 \text{ nm}$), two different broadband (**F**) spectra reconstructed with our spectrometer (solid) and measured using a commercial spectrometer (dashed). **G**, Peak signal-to-noise ratio between reconstructed and reference spectra as a function of learning step.

tively, and P is the incident light power (Fig. S8). The gate-tunable spectral response with high sensitivity over a wide spectral range is due to the wavelength-dependent absorption (29) of MoS₂ and WSe₂ as well as the controllable charge carrier transport (22–28) through the MoS₂/WSe₂ interface, unlike the individual material. The spectral response matrix (Fig. 2D) inherits a rich structure from the dynamics of photoexcited charge carriers generated across the tunable MoS₂/WSe₂ heterojunction (22–29), confirming fast and stable spectral detection with giant gate-tunability in our MoS₂/WSe₂ heterojunction (Figs. S9 to S13).

After encoding this spectral response matrix (Fig. 2D) for the learning process, our single-junction spectrometer is ready to measure unknown incident light spectra, following the workflow diagram (Fig. S2). Briefly, we measure the gate-tunable photocurrent of the unknown incident light and then compute its constrained least-square solution to reconstruct the spectrum using adaptive Tikhonov regularization by minimizing the residual norm with a regularization factor (I , 8). Details of the optical setup, electrical/optoelectrical measurements, and computational reconstruction are provided in Fig. S14 and sections MM2 to MM4.

The quasi-monochromatic and complex broadband spectra reconstructed with our single-junction spectrometer agree well with the reference spectra measured using a commercial spectrometer, demonstrating the viability of single-junction spectrometer concept (Fig. 2, E and F). While the demonstrated bandwidth (from ~ 405 to 845 nm) is limited due to the availability of the light wavelengths in our laboratory, the MoS₂/WSe₂ heterojunction exhibits photoreponse from ~ 400 to 2400 nm (25). Indeed, the vdW junctions are known to exhibit photodetection capability for incident light whose wavelength corresponds to around half (or even much smaller than) the bandgap of each material (15–17, 25). Therefore, in principle, single-junction spectrometer is not limited by the material bandgap and likely offers operation bandwidth broader than our demonstration. Our single-junction spectrometer using the interlayer-transport-mediated photoresponse is fundamentally different from the previously demonstrated

spectrometer concepts, such as bandgap engineering and grading (7–10). Detailed comparisons of our work with the current state-of-the-art miniaturized spectrometers (including black-phosphorus-based spectrometers with the Stark effect (9)) are given in section ST2 and table S1.

To evaluate deviations between the reconstructed and reference spectra, the peak signal-to-noise ratio (PSNR) has previously been used to analyze the mean squared error (section ST3). The maximum PSNR estimated from the extrapolation is ~ 35.7 and 33.6 dB for the quasi-monochromatic and complex broadband spectra, respectively (Fig. 2G). A reasonable learning step (i.e. step in wavelength for encoding the spectral response matrix) can be chosen based on the saturated PSNR. Therefore, a high-speed learning process is achievable with a large learning step and slightly reduced accuracy (11).

The wavelength resolving power is an important measure of spectrometers in practical applications (1, 2). To demonstrate high spectral resolution capability with our single-junction ultra-miniaturized spectrometer, we construct a high-density spectral response matrix through an ultra-small learning step of ~ 0.1 nm using monochromatic light from ~ 675 nm to 685 nm for the learning process (Fig. 3A). Our single-junction spectrometer encoded by the high-density spectral response matrix can resolve monochromatic light with high accuracy (Fig. 3, B and C). The average peak wavelength difference ($\Delta\lambda$) between reconstructed and reference spectra is $\sim 0.36 \pm 0.06$ nm, with a minimum of ~ 0.04 nm (Fig. 3D). This is comparable to the learning step of ~ 0.1 nm. The wavelength resolving power ($R_\lambda = \frac{\lambda}{\Delta\lambda}$) at a given input wavelength (λ) is $\sim 3470 \pm 880$.

Furthermore, we measure complex incident spectra to study spectral resolution. Two peaks at ~ 679 nm, separated by ~ 3 nm, are successfully distinguished (Fig. 3E). Our spectrometer can also resolve broadband spectra and identify their peak wavelengths with high resolution (~ 0.9 nm demonstrated in Fig. S15). This indicates that our spectrometer has spectral resolu-

tion comparable to or better than the current state-of-the-art miniaturized spectrometers (*I–II*) with footprint ($\sim 22 \times 8 \mu\text{m}^2$) comparable to or smaller than most. This is several orders of magnitude smaller than commercial miniaturized spectrometers (*30*) and recently demonstrated spectrometers with metasurfaces (*4*), quantum dots (*6*), or a single-dot perovskite (*10*); see Table S1 for a detailed comparison. We note that the demonstrated accuracy ($\sim 0.36 \text{ nm}$) and

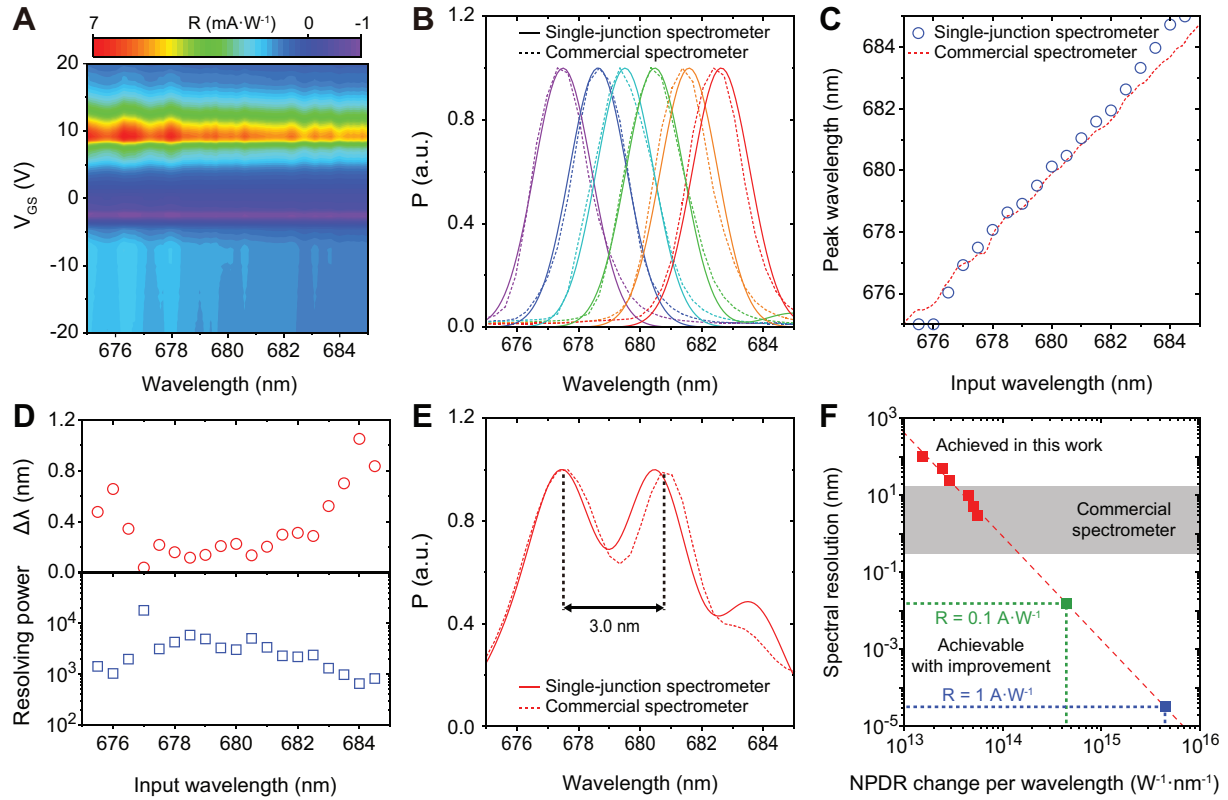


Figure 3: High-performance wavelength resolving power and spectral resolution. **A**, Color contour plot of the high-density spectral response matrix with a learning step of $\sim 0.1 \text{ nm}$. **B**, Monochromatic (bandwidth: $\sim 2 \text{ nm}$) spectra reconstructed with our spectrometer (solid) and measured using a commercial spectrometer (dashed). **C**, Peak wavelengths of the reconstructed and measured spectra as a function of input wavelength. **D**, Peak wavelength difference between reconstructed and reference spectra (upper panel), and wavelength resolving power of our single-junction spectrometer (lower panel). **E**, Complex spectra reconstructed (solid) and measured (dashed). **F**, Future prospect of our single-junction spectrometer aiming for ultra-high-resolution.

resolution (~ 3 nm), which are limited by the smallest incident wavelength step available in our laboratory, can be further improved by minimizing the learning step during the learning process. We suggest that such a learning process is practical for applications, similar to the calibration process in traditional spectrometers.

Many strategies can be considered to improve the resolution, accuracy, and speed of our single-junction spectrometer (1). These include: (A) increasing the dataset size to create higher-density spectral response matrix by minimizing the learning step (7–11), (B) designing junctions with higher response and larger wavelength or gate dependence (15–17), and (C) optimizing the reconstruction algorithm (e.g., suppressing the perturbation with more advanced regularization (1, 8) or increasing the accuracy with convolutional processing (20, 21)). Ideally, decreasing the learning step is a straightforward approach to forming a denser spectral response matrix for more accurate spectral reconstruction. However, there is a trade-off: signal difference, measured at small learning steps, comparable to the measurement noise could result in errors during reconstruction.

To illustrate the future development possibilities of single-junction spectrometers, we consider the normalized photocurrent-to-dark current ratio (NPDR) change per wavelength step of two resolved peaks (section ST4). The extrapolated line in Fig. 3F indicates the potential of our approach with improved photoresponsivity for higher resolution than the commercial miniaturized spectrometers (30). The achievable resolution is highlighted based on recently reported photoresponse (~ 0.1 to $1 \text{ A}\cdot\text{W}^{-1}$ at 532 nm) of $\text{MoS}_2/\text{WSe}_2$ heterojunctions (25). The resolution and bandwidth can be further improved by engineering junctions with different combinations of various 2D materials or integrating waveguides (15–17). Additional strategies for improving performance are provided in section ST5. With a significant potential to improve performance, our single-junction spectrometer can not only be adapted to other tunable junction architectures but also integrated with CMOS (complementary metal-oxide-semiconductor)-

compatible platforms.

Our single-junction spectrometer can benefit from the recently developed large-scale 2D material synthesis to construct an array for future spectral imaging. Here, we demonstrate proof-of-concept spectral imaging of a color filter consisting of red, blue, and transparent areas with spatial scanning using our spectrometer (Fig. 4A). At each mapping position, the measured photocurrent data at different V_{GS} are recorded in the spatial response data cube for spectral reconstruction. A series of photocurrent mapping data scanned at different V_{GS} is displayed (Fig. 4B) and converted to a series of spectral data reconstructed at different wavelengths (Fig. 4C). The

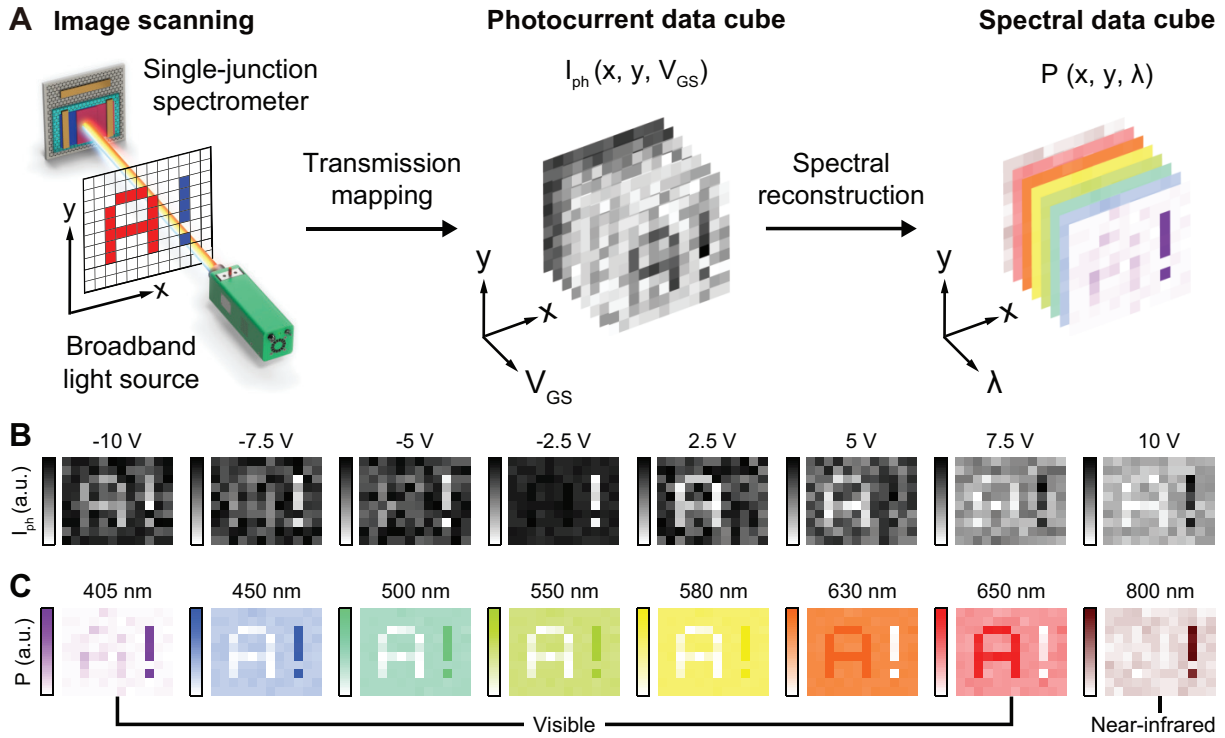


Figure 4: **Proof-of-concept demonstration of spectral imaging.** **A**, Configuration of spectral imaging using our single-junction spectrometer with a spatial scanning method. A broadband light source filtered with a color image is incident to our spectrometer for spectral imaging. **B**, Photocurrent mapping data scanned at different V_{GS} . **C**, Spectral images reconstructed at different wavelengths, covering the visible to near-infrared ranges. Higher intensity at each wavelength indicates more broadband light is transmitted through the color image. The pixel intensity in **B** and **C** is normalized with each maximum intensity.

spectral images indicate that the red and blue filters absorb more incident broadband light from ~ 405 to 580 nm, and from ~ 600 to 700 nm, respectively. As a result, the spectra of the red uppercase alphabet "A" (from ~ 450 to 700 nm) and the blue exclamation mark "!" (from ~ 405 to 845 nm) are distinguishable from that of the background. Note that a strong light signal at near 800 nm for the exclamation mark "!" can be fully detected, highlighting the advantages of spectral imaging over conventional RGB color imaging (Fig. S16 with different color filters). In our demonstration, the image resolution is defined by the mapping step. However, our concept has great potential for large-scale spectral imaging by future array devices, offering high spatial resolution with the junction at the micrometer- or nanometer-scale.

In our spectrometer, no photodetector array, filter array, or other bulky dispersive components are required to achieve high resolution, sub-nm accuracy, and broad operation bandwidth. The compact footprint of our single-junction spectrometers may provide scalability and compatibility with the current photonic integrated circuits and CMOS-compatible processes for direct integration into modern smartphones, lab-on-a-chip systems, and other customized devices ranging from bio-implants to drones and satellites.

References

1. Z. Yang, T. Albrow-Owen, W. Cai, T. Hasan, Miniaturization of optical spectrometers. *Science* **371**, eabe0722 (2021).
2. R. F. Wolffenbuttel, State-of-the-art in integrated optical microspectrometers. *IEEE Trans. Instrum. Meas.* **53**, 197-202 (2004).
3. Z. Wang et al., Single-shot on-chip spectral sensors based on photonic crystal slabs. *Nat. Commun.* **10**, 1020 (2019).

4. A. Tittl et al., Imaging-based molecular barcoding with pixelated dielectric metasurfaces. *Science* **360**, 1105-1109 (2018).
5. D. M. Kita et al., High-performance and scalable on-chip digital Fourier transform spectroscopy. *Nat. Commun.* **9**, 4405 (2018).
6. J. Bao, M. G. Bawendi, A colloidal quantum dot spectrometer. *Nature* **523**, 67-70 (2015).
7. J. Meng, J. J. Cadusch, K. B. Crozier, Detector-only spectrometer based on structurally colored silicon nanowires and a reconstruction algorithm. *Nano Lett.* **20**, 320-328 (2019).
8. Z. Yang et al., Single-nanowire spectrometers. *Science* **365**, 1017-1020 (2019).
9. S. Yuan, D. Naveh, K. Watanabe, T. Taniguchi, F. Xia, A wavelength-scale black phosphorus spectrometer. *Nat. Photonics* **15**, 601-607 (2021).
10. L. Guo et al., A single-dot perovskite spectrometer. *Adv. Mater.*, 2200221 (2022).
11. L. Kong et al., Single-detector spectrometer using a superconducting nanowire. *Nano Lett.* **21**, 9625-9632 (2021).
12. F. Xia, T. Mueller, Y.-m. Lin, A. Valdes-Garcia, P. Avouris, Ultrafast graphene photodetector. *Nat. Nanotechnol.* **4**, 839-843 (2009).
13. M. Buscema et al., Photocurrent generation with two-dimensional van der Waals semiconductors. *Chem. Soc. Rev.* **44**, 3691-3718 (2015).
14. F. Koppens et al., Photodetectors based on graphene, other two-dimensional materials and hybrid systems. *Nat. Nanotechnol.* **9**, 780-793 (2014).
15. A. K. Geim, I. V. Grigorieva, Van der Waals heterostructures. *Nature* **499**, 419-425 (2013).

16. M. M. Furchi, A. Pospischil, F. Libisch, J. Burgdörfer, T. Mueller, Photovoltaic effect in an electrically tunable van der Waals heterojunction. *Nano Lett.* **14**, 4785-4791 (2014).
17. N. Ubrig et al., Design of van der Waals interfaces for broad-spectrum optoelectronics. *Nat. Mater.* **19**, 299-304 (2020).
18. S. Wang et al., Nonvolatile van der Waals heterostructure phototransistor for encrypted optoelectronic logic circuit. *ACS Nano* **16**, 4528-4535 (2022).
19. Y. Sun, Y. Ding, D. Xie, Mixed-dimensional van der Waals heterostructures enabled optoelectronic synaptic devices for neuromorphic applications. *Adv. Funct. Mater.* **31**, 2105625 (2021).
20. S. Lee, R. Peng, C. Wu, M. Li, Programmable black phosphorus image sensor for broadband optoelectronic edge computing. *Nat. Commun.* **13**, 1485 (2022).
21. L. Pi et al., Broadband convolutional processing using band-alignment-tunable heterostructures. *Nat. Electron.* **5**, 248-254 (2022).
22. C.-H. Lee et al., Atomically thin p-n junctions with van der Waals heterointerfaces. *Nat. Nanotechnol.* **9**, 676-681 (2014).
23. T. Roy et al., Dual-gated MoS₂/WSe₂ van der Waals tunnel diodes and transistors. *ACS Nano* **9**, 2071-2079 (2015).
24. A. Nourbakhsh, A. Zubair, M. S. Dresselhaus, T. Palacios, Transport properties of a MoS₂/WSe₂ heterojunction transistor and its potential for application. *Nano Lett.* **16**, 1359-1366 (2016).
25. M. Long et al., Broadband photovoltaic detectors based on an atomically thin heterostructure. *Nano Lett.* **16**, 2254-2259 (2016).

26. Y. Son et al., Observation of switchable photoresponse of a monolayer WSe₂-MoS₂ lateral heterostructure via photocurrent spectral atomic force microscopic imaging. *Nano Lett.* **16**, 3571-3577 (2016).
27. M.-H. Doan et al., Charge transport in MoS₂/WSe₂ van der Waals heterostructure with tunable inversion layer. *ACS Nano* **11**, 3832-3840 (2017).
28. X. Sun et al., Visualizing Band Profiles of Gate-Tunable Junctions in MoS₂/WSe₂ Heterostructure Transistors. *ACS Nano* **15**, 16314-16321 (2021).
29. H. S. Ra et al., An Asymmetry Field-Effect Phototransistor for Solving Large Exciton Binding Energy of 2D TMDCs. *Adv. Mater.* **34**, 2107468 (2022).
30. *Mini-spectrometers product lineup* (Hamamatsu, 2022); <https://www.hamamatsu.com/eu/en/product/optical-sensors/spectrometers/mini-spectrometer.html>
31. H. H. Yoon et al., Strong fermi-level pinning at metal/n-Si (001) interface ensured by forming an intact Schottky contact with a graphene insertion layer. *Nano Lett.* **17**, 44-49 (2017).
32. S. Jung et al., Reduction of water-molecule-induced current-voltage hysteresis in graphene field effect transistor with semi-dry transfer using flexible supporter. *J. Appl. Phys.* **125**, 184302 (2019).
33. H. H. Yoon et al., Negative Fermi-level pinning effect of metal/n-GaAs (001) junction induced by a graphene interlayer. *ACS Appl. Mater. Interfaces* **11**, 47182-47189 (2019).
34. F. Pizzocchero et al., The hot pick-up technique for batch assembly of van der Waals heterostructures. *Nat. Commun.* **7**, 11894 (2016).

35. R. Frisenda et al., Recent progress in the assembly of nanodevices and van der Waals heterostructures by deterministic placement of 2D materials. *Chem. Soc. Rev.* **47**, 53-68 (2018).
36. K. Kinoshita et al., Dry release transfer of graphene and few-layer h-BN by utilizing thermoplasticity of polypropylene carbonate. *npj 2D Mater. Appl.* **3**, 22 (2019).
37. L. Britnell et al., Field-effect tunneling transistor based on vertical graphene heterostructures. *Science* **335**, 947-950 (2012).
38. F. Ahmed et al., Dielectric dispersion and high field response of multilayer hexagonal boron nitride. *Adv. Funct. Mater.* **28**, 1804235 (2018).
39. M. Faraji-Dana et al., Compact folded metasurface spectrometer. *Nat. Commun.* **9**, 4196 (2018).
40. E. Le Coarer et al., Wavelength-scale stationary-wave integrated Fourier-transform spectrometry. *Nat. Photonics* **1**, 473-478 (2007).
41. H. Sun et al., In situ formed gradient bandgap-tunable perovskite for ultrahigh-speed color/spectrum-sensitive photodetectors via electron-donor control. *Adv. Mater.* **32**, 1908108 (2020).
42. Y. Liu et al., Van der Waals heterostructures and devices. *Nat. Rev. Mater.* **1**, 16042 (2016).
43. K. Novoselov, o. A. Mishchenko, o. A. Carvalho, A. Castro Neto, 2D materials and van der Waals heterostructures. *Science* **353**, aac9439 (2016).
44. D. Jariwala, T. J. Marks, M. C. Hersam, Mixed-dimensional van der Waals heterostructures. *Nat. Mater.* **16**, 170-181 (2017).

45. G. Konstantatos, Current status and technological prospect of photodetectors based on two-dimensional materials. *Nat. Commun.* **9**, 5266 (2018).
46. L. Pahun, Y. Campidelli, F. A. d'Avitaya, P. Badoz, Infrared response of Pt/Si/ErSi_{1.7} heterostructure: tunable internal photoemission sensor. *Appl. Phys. Lett.* **60**, 1166-1168 (1992).
47. P. Vabbina et al., Highly sensitive wide bandwidth photodetector based on internal photoemission in CVD grown p-type MoS₂/graphene Schottky junction. *ACS Appl. Mater. Interfaces* **7**, 15206-15213 (2015).
48. H. Yang et al., Graphene barristor, a triode device with a gate-controlled Schottky barrier. *Science* **336**, 1140-1143 (2012).
49. Y. J. Choi et al., Color-selective Schottky barrier modulation for optoelectric logic. *ACS Nano* **14**, 16036-16045 (2020).
50. H. H. Yoon et al., Tunable Quantum Tunneling through a Graphene/Bi₂Se₃ Heterointerface for the Hybrid Photodetection Mechanism. *ACS Appl. Mater. Interfaces* **13**, 58927-58935 (2021).
51. M. Du et al., Switchable photoresponse mechanisms implemented in single van der Waals semiconductor/metal heterostructure. *ACS Nano* **16**, 568-576 (2022).
52. X. Bai et al., Molybdenum disulfide/double-wall carbon nanotube mixed-dimensional heterostructures. *Adv. Mater. Interfaces* **9**, 2200193 (2022).
53. N. Li et al., van der Waals semiconductor empowered vertical color sensor. *ACS Nano* **16**, 8619-8629 (2022).

54. G. Jin et al., Heteroepitaxial van der Waals semiconductor superlattices. *Nat. Nanotechnol.* **16**, 1092-1098 (2021).
55. W. Zhang, Q. Wang, Y. Chen, Z. Wang, A. T. Wee, Van der Waals stacked 2D layered materials for optoelectronics. *2D Mater.* **3**, 022001 (2016).
56. S. Goossens et al., Broadband image sensor array based on graphene–CMOS integration. *Nat. Photonics* **11**, 366-371 (2017).
57. W. Liu et al., Graphene charge-injection photodetectors. *Nat. Electron.* **5**, 281-288 (2022).
58. C. Gong et al., 2D nanomaterial arrays for electronics and optoelectronics. *Adv. Funct. Mater.* **28**, 1706559 (2018).
59. J. Li et al., General synthesis of two-dimensional van der Waals heterostructure arrays. *Nature* **579**, 368-374 (2020).
60. L. Mennel et al., Ultrafast machine vision with 2D material neural network image sensors. *Nature* **579**, 62-66 (2020).
61. C. Kim et al., Fermi level pinning at electrical metal contacts of monolayer molybdenum dichalcogenides. *ACS Nano* **11**, 1588-1596 (2017).
62. J. Jang et al., Fermi-Level Pinning-Free WSe₂ Transistors via 2D van der Waals metal contacts and their circuits. *Adv. Mater.* **34**, 2109899 (2022).
63. X. Liu, M. S. Choi, E. Hwang, W. J. Yoo, J. Sun, Fermi level pinning dependent 2D semiconductor devices: challenges and prospects. *Adv. Mater.* **34**, 2108425 (2022).
64. J. Xiao, M. Zhao, Y. Wang, X. Zhang, Excitons in atomically thin 2D semiconductors and their applications. *Nanophotonics* **6**, 1309-1328 (2017).

65. M. Massicotte et al., Dissociation of two-dimensional excitons in monolayer WSe₂. *Nat. Commun.* **9**, 1633 (2018).
66. H. H. Yoon, W. Cai, F. Nigmatulin, Spectral Reconstruction Based on Tunable vdW Junction Spectrometers, version 1.0, Zenodo (2022) <https://doi.org/10.5281/zenodo.7012876>.

Acknowledgments

We acknowledge the provision of facilities and technical support from the Otaniemi research infrastructure (OtaNano-Micronova Nanofabrication Centre and OtaNano-Nanomicroscopy Centre). We thank Andreas Liapis, Mingde Du, Yunyun Dai, Suvi-Tuuli Akkanen, Juan Camilo Arias, and Xueyin Bai for valuable discussions and Mikko Turunen, Diao Li, Yi Zhang, Vincent Pelgrin, and Susobhan Das for access to the optical instruments and components. **Funding:** This work was supported by the Academy of Finland (Grant No. 314810, 333982, 336144, 336813, 336818, and 348920), Academy of Finland Flagship Programme (Grant No. 320167, PREIN), the EU H2020-MSCA-RISE-872049 (IPN-Bio), EPSRC (Grant No. EP/T014601/1), ERC (Grant No. 834742), and National Natural Science Foundation of China (Grant No. 51976122 and 52061135108). Pertti Hakonen was supported by the Jane and Aatos Erkko foundation and the Technology Industries of Finland centennial foundation (Future Makers 2021). **Author contributions:** Z.S. conceived the ideas during the discussion with H.H.Y. and F.A.. H.H.Y. designed the experiments and carried out the characterizations/measurements. H.H.Y., H.A.F., F.N., and M.G.U. fabricated the van der Waals heterostructures and spectrometer devices. H.A.F. provided the home-built optical system and prepared the optical instruments and components. F.A. and X.C. helped with the electrical and optoelectrical measurements. H.H.Y., F.N., W.C., Z.Y., and H.C. developed the reconstruction code. W.C., Z.Y.,

H.C., and T.H. shared the processing strategies. H.H.Y., H.A.F., F.N., F.A., and Z.S. analyzed the data. W.C., E.D.M., P.H., K.K., H.L., and T.H. commented on the experimental results and helped with the data analysis. H.A.F. and X.C. helped with the graphic design. H.H.Y. wrote the manuscript, and Z.S. supervised the research. All authors participated in the scientific discussion extensively and contributed to the manuscript writing. **Correspondence:** addressed to H.H.Y. or Z.S.. **Competing interests:** The authors declare no competing interests. **Data and materials availability:** All data needed to evaluate the conclusions in the paper are present in the main text or the supplementary materials. Code used for spectral reconstruction based on tunable vdW junction spectrometers is available at <https://github.com/fonig/Reconstruction> and archived at Zenodo (66).

Supplementary Material

Materials and Methods

Supplementary Text

Figs. S1 to S16

Table S1

References (31-66)